

Investigation of the blast-resistance performance of geotextile-reinforced soil

S.-C. Tseng¹, K.-H. Yang², Y.-K. Tsai³ and F.-C. Teng⁴

¹Ph.D. Candidate, Department of Civil and Construction Engineering, National Taiwan University of Science and Technology (Taiwan Tech), Taipei, Taiwan, E-mail: d10505002@mail.ntust.edu.tw

²Professor, Department of Civil Engineering, National Taiwan University (NTU), Taipei, Taiwan, E-mail: khyang@ntu.edu.tw (corresponding author)

³Associate Professor, Department of Environmental Information and Engineering, Chung Cheng Institute of Technology, National Defense University (NDU), Taoyuan, Taiwan, E-mail: jeremysai0406@nycu.edu.tw

⁴Associate Professor, Department of Civil and Construction Engineering, National Taiwan University of Science and Technology (Taiwan Tech), Taipei, Taiwan, E-mail: fteng@mail.ntust.edu.tw

Received 13 April 2022, accepted 03 July 2022

ABSTRACT: An explosion on the ground surface can cause considerable damage to underground structures. In this study, a series of experimental and numerical investigations were conducted to examine the performance and reinforcing mechanism of reinforced soil subjected to blast loads. An excavated pit backfilled with sand only (unreinforced soil) and sand reinforced with three layers of geotextiles (reinforced soil) were used as test models in a field explosion test. In the field explosion test, blast pressures in air and soil, ground deformation, and mobilized reinforcement tensile strain were measured. The test results obtained for the reinforced and unreinforced soil were compared to evaluate the effectiveness of using soil reinforcement as a protective barrier against blast loads. The test results indicated that peak blast pressure in the reinforced soil was only 10–28% of those in the unreinforced soil. Two reinforcing mechanisms were identified in this study: the tensioned membrane effect and lateral restraint effect. Moreover, a series of numerical analyses were performed to evaluate the effects of reinforcement parameters on the blast pressure. This study provides useful insights into the application and design of soil reinforcement as an alternative antiexplosion measure to protect underground structures against surface explosions.

KEYWORDS: Geosynthetics, reinforced soil, blast loads, tensioned membrane effect

REFERENCE: Tseng, S.-C., Yang, K.-H., Tsai, Y.-K. and Teng, F.-C. (2022). Investigation of the blast-resistance performance of geotextile-reinforced soil. *Geosynthetics International*. [<https://doi.org/10.1680/jgein.22.00269>]

1. INTRODUCTION

An explosion on the ground surface can cause considerable damage to underground structures, such as basements, tunnels, pipelines, fuel storage tanks, and ammunition depots. The extent of damage depends on the intensity of the explosion, the material and configuration of the structure, the distance between the explosion source and the structure, and the properties of the intervening subsurface deposit (Woods and Jedelet 1985; De *et al.* 2016). A protective barrier can be installed directly above underground structures to mitigate the effects of surface explosions on these structures. The backfill materials used in such protective barriers are typically ductile, compressible, and reinforced materials. The characteristics of backfill materials, including their property,

density, and thickness, play crucial roles in attenuating the stresses caused by surface blasts.

Experimental and numerical studies have proven that the use of soil with geosynthetic materials as backfill materials in protective barriers, such as geofoams (Wang *et al.* 2006; Ossa and Romo 2009; Anil *et al.* 2015; AbdelSalam and Azzam 2016; De *et al.* 2016; De and Zimmie 2016; Witthoef and Kim 2016; Baziar *et al.* 2018; Zhao *et al.* 2021; Khodaparast *et al.* 2022), geocells (Hegde and Sitharam 2015; Babagiray *et al.* 2016; Fattah and Redha 2016), and geotextiles or geogrids (Tupa and Palmeira 2007; Palmeira and Andrade 2010; Vivek and Sitharam 2017; Dave and Solanki 2020; Pires and Palmeira 2021), can effectively absorb the energy of surface explosions or dynamic impacts and thus mitigate the effects of these phenomena on underground structures.

Studies were also conducted to investigate the deformation characteristics of geomembranes subjected to gas pressure (Xu *et al.* 2017; Wang *et al.* 2021) and geotextiles subjected to ballistic impact (Martínez-Hergueta *et al.* 2022, 2017).

Reinforced soil possesses high energy absorption capacity and impact resistance. In addition to conventional applications, geosynthetic-reinforced soil (GRS) structures have recently been used as barriers for resisting lateral impact forces associated with natural disasters, such as floods, tsunamis, rock falls, debris flows, and avalanches (Recio-Molina and Yasuhara 2005; Choudhury and Ahmad 2007; Peila *et al.* 2007; Yasuhara and Recio-Molina 2007; Lambert *et al.* 2009; Ronco *et al.* 2009; Brandl 2011; Fowze *et al.* 2012; Kuwano *et al.* 2012; Lambert and Bourrier 2013; Koseki and Shibuya 2014; Yang *et al.* 2016b, 2020; Cuomo *et al.* 2020; Watanabe *et al.* 2020; Liu *et al.* 2021). The impact of lateral loadings from traffic on reinforced structures has also been investigated (Kim *et al.* 2010; Soude *et al.* 2013). In general, the aforementioned studies have concluded that because of the flexible nature of reinforced soil, it can effectively resist lateral impact forces from natural disasters or traffic, therefore maintaining system stability. Soil reinforcement techniques have also been used in military applications to protect personnel and property from explosions. Compared with conventional reinforced concrete structures, the merits of soil reinforcement are faster construction, higher mobility, lower labor requirements, higher tolerance of differential settlement, and greater extent of ductile failure without fragmentation upon blast impact. However, limited studies have investigated the performance and effectiveness of reinforced soil against blast loads (Yogendrakumar and Bathurst 1992; Pieri 1998; Ng *et al.* 2000; Tupa and Palmeira 2007; Tuan 2014; Vivek and Sitharam 2017; Dave and Solanki 2020).

Tupa and Palmeira (2007) conducted reduced-scale model tests to evaluate the capacity of geosynthetics to minimize the damage caused by the explosions of internally pressurized buried pipes. Their results revealed that geotextiles enabled the smooth spreading of the air bursting out from the pipes, which reduced the air burst pressure transferred to the soil and consequently minimized the movement of the soil mass within the influence zone. Vivek and Sitharam (2017) performed laboratory experiments to study the performance of geotextile-encapsulated sand barrier systems in mitigating shock waves. Their results indicated that the geotextile considerably reduced gas pressure (to one-third of the pressure in the unreinforced case) in a gradual manner (i.e. with a low rate of pressure decrease). The geotextile prevented direct contact between the shock wave and sand particles, thereby reducing the magnitude of the transferred stress. Dave and Solanki (2020) reviewed the effects of geosynthetic reinforcement on buried pipes subjected to different loading conditions, including static load, repeated load, permanent ground deformation, accidental damage, uplift pressure, and explosion. Their study indicated that the introduction of geosynthetic reinforcement effectively reduced the stress, strain, deflection, and vibration in the

pipes. Yogendrakumar and Bathurst (1992) conducted finite element analyses to investigate the dynamic response of GRS structures subjected to blast loading. They found that the reinforcement improved the performance of the structures under blast loading by reducing the permanent soil deformation by 30%. Pieri (1998) performed full-scale tests on three blast-mitigation walls and found that the GRS wall reduced the blast pressure by approximately 42% compared with that in a test conducted without any protective measure. Ng *et al.* (2000) conducted full-scale tests to evaluate the performance of GRS walls with rigid and flexible facings that were subjected to multiple blasts. They found that the GRS walls impeded the propagation of blasts at the ground level and absorbed high levels of energy because of their tolerance for deformation.

Few studies have demonstrated soil reinforcement as a valid mitigation measure against blast loads. In particular, the effects of reinforcement parameters on the performance of reinforced soil subjected to blast loads have not been fully investigated. Furthermore, the mobilized reinforcement tensile force caused by blast loads, crucial information for understanding the reinforcing mechanism, has not been examined in previous studies. Therefore, in this study, a series of experimental tests and numerical analyses were conducted to investigate the performance of reinforced soil as a protective barrier against surface blasts. The specific objectives of this study were to (1) investigate the blast-resistance performance of reinforced soil, (2) examine the mobilized reinforcement tensile force caused by blast loads for understanding the reinforcing mechanism against surface blasts, (3) evaluate the influence of reinforcement parameters (i.e. number of reinforcement layers, ultimate tensile strength, and stiffness) on the attenuation of the peak blast pressure, and (4) provide suggestions for the use of soil reinforcement as a protective barrier against surface blasts. The field explosion tests conducted in the present study are first introduced. The test model, soil and reinforcement materials, test procedure, and test results are discussed. The numerical models are then introduced. The numerical models were validated using the field test results. After model validation, a series of parametric studies were conducted to evaluate the influence of reinforcement parameters on the blast-resistance performance of reinforced soil. On the basis of the test and numerical results, suggestions and design implications for the use of soil reinforcement as a protective barrier against surface blasts are provided.

2. FIELD EXPLOSION TEST

2.1. Test models

Figure 1 illustrates an underground protective structure suggested by the TM 5-855-1 manual of the US military (USDA 1998). This protective barrier is composed of a concrete burster slab or rock rubble overlay to prevent the penetration of artillery shells, and an attenuation layer composed of backfill material to reduce the blast pressure.

The attenuation layer is typically backfilled with a 15 to 180 cm thick sand, as suggested by the UFC 3-340-02 manual of the US military (USDA 2008). This study focuses on the attenuation layer with an aim to reduce its thickness by using reinforced soil.

Field explosion tests were performed at a military training ground of the Military Academy, Taiwan. Two test models were constructed: one comprising sand only (unreinforced soil) and another containing sand reinforced with three layers of geotextiles (reinforced soil). Figure 2 presents the test layout and instrumentation setup for the reinforced soil. The unreinforced soil had a similar layout to the reinforced soil except that no reinforcement was installed. The in-situ soil is poorly graded sand with silt, classified as SP-SM according to the Unified Soil Classification System (USCS; Wang 2021).

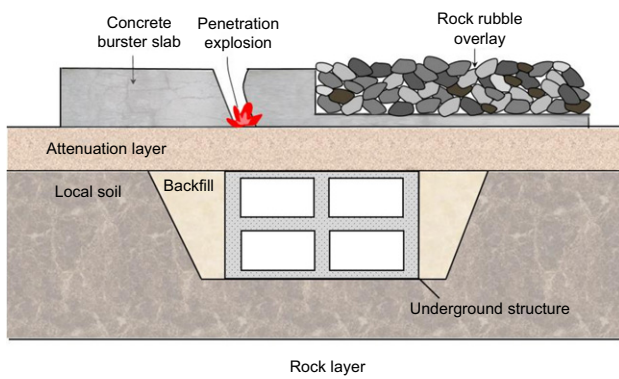


Figure 1. Illustration of a typical underground protective structure (redrawn from US military manual No. TM 5-855-1 (USDA 1998))

A test pit with dimensions of 100 × 100 × 60 cm (length × width × depth) was excavated and backfilled with uniform quartz sand for better controlling the soil density and quality. Three geotextile layers were placed with a vertical spacing of 20 cm. Sandbags were installed inside at both ends of the test pit and enfolded by the geotextile layers to form wrap-around ends. A quarter pound (= 113 g) of trinitrotoluene (TNT) explosive with cylindrical shape was placed on top of the test models, and explosions were conducted twice for each test model.

Table 1 lists the scale effect considered in the explosion tests. The similarity of explosions followed the Hopkinson–Cranz (or cube-root) scaling law (Baker *et al.* 1973), which is expressed as follows:

$$Z_s = \frac{R}{W^{1/3}} \quad (1)$$

where Z_s is the scaled distance, R is the distance from the center of the explosive charge to the target (or the thickness of the attenuation layer in this study), W is the weight of the explosive charge. Equation 1 indicates that two explosions with different quantities of explosive charges can produce similar blast waves at two scaled distances. For example, a model test with $W = 0.113$ kg at $R = 0.6$ m and a prototype test with $W = 3.0$ kg at $R = 1.8$ m have similar explosion effects because both model and prototype tests produce $Z_s = 1.24$.

2.2. Material properties

The soil used in the explosion tests was uniform quartz sand, which is classified as poorly graded sand (SP) according to the USCS. Figure 3 displays the grain size distribution curve of the sand used in the explosion tests.

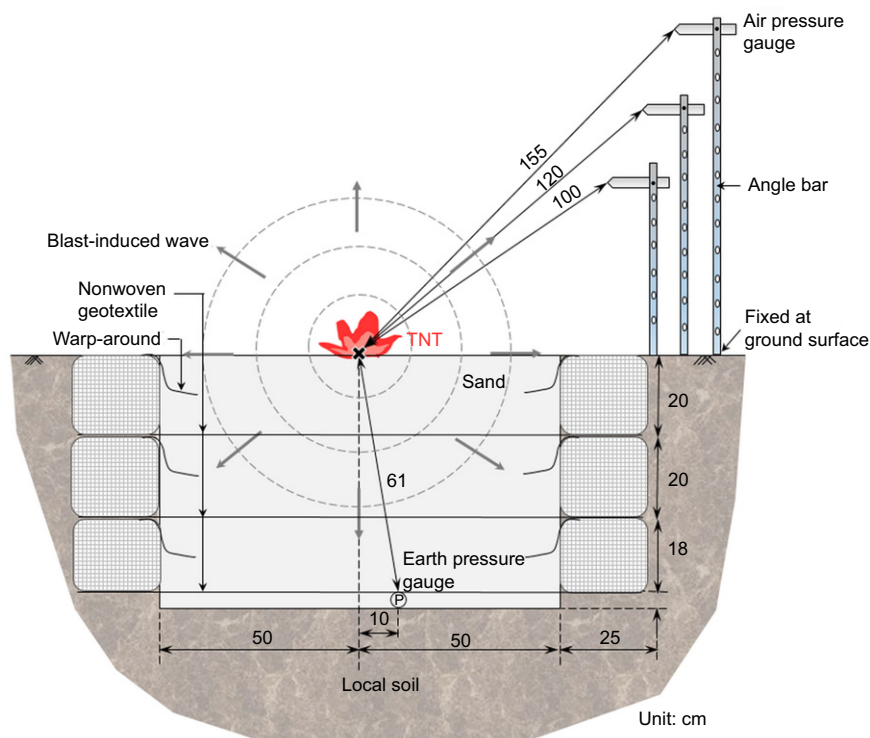


Figure 2. Explosion test layout and instrumentation setup

Table 1. Scale effect for the explosion tests

Model/Prototype	TNT weight, W (kg)	Distance from TNT, R (m)	Scaled distance, $Z_s = R/W^{1/3}$ (kg/m ³)
Model test	0.113	0.6	1.24
Target prototype	3.0	1.8	1.24

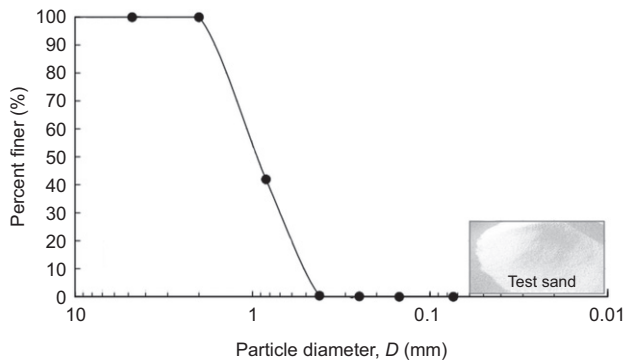


Figure 3. Grain size distribution of the test sand

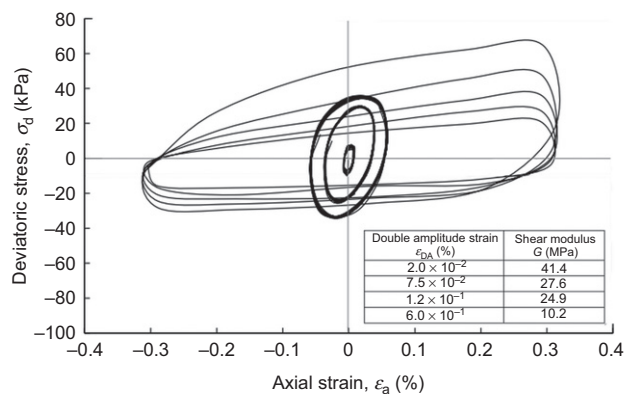


Figure 4. Dynamic behavior of the test sand under cyclic triaxial tests

Table 2 summarizes the soil properties, which were determined in line with ASTM standards. The sand used in the tests had a specific gravity $G_s = 2.67$, a mean particle size $D_{50} = 0.95$ mm, a minimum dry unit weight $\gamma_{d,\min} = 15.5$ kN/m³, and a maximum dry unit weight $\gamma_{d,\max} = 17$ kN/m³. The soil unit weight was $\gamma = 16.04$ kN/m³ at the target relative density $D_r = 40\%$. The soil shear strength properties were cohesion $c' = 0$ kN/m² and peak friction angle $\phi' = 37^\circ$, obtained through consolidated-drained triaxial compression tests. The soil dynamic behavior was determined through cyclic triaxial tests (ASTM D3999). Sand specimens were tested under incrementally increasing strain levels. For each strain level, uniform sinusoidal deformation was achieved at a frequency of 1 Hz through five loading cycles. Figure 4 shows the results of the cyclic triaxial tests. The soil shear modulus was calculated from the stress-strain hysteresis loop. The test results indicated that the soil shear modulus decreased from $G = 41.4$ to 10.2 MPa as the strain level increased.

Table 2. Properties of test sand

Parameter	Value
Index property	
Unified soil classification system	SP
Specific gravity, G_s	2.67
D_{10} (mm)	0.52
D_{30} (mm)	0.71
D_{60} (mm)	1.25
Coefficient of curvature, C_c	4.5
Coefficient of uniformity, C_u	2.37
Unit weight	
Minimum dry unit weight, $\gamma_{d,\min}$ (kN/m ³)	15.5
Maximum dry unit weight, $\gamma_{d,\max}$ (kN/m ³)	17
Unit weight, γ (kN/m ³)	16.04
Shear strength and stiffness	
Cohesion, c' (kPa)	0
Friction angle, ϕ' ($^\circ$)	37
Bulk modulus, K (MPa)	525.4
Shear modulus, G (MPa)	refer to Figure 4

The reinforcement used in the explosion test was needle-punched polyethylene terephthalate nonwoven geotextile. The density and thickness of this geotextile were 200 g/m² and 1.78 mm, respectively. Tupa and Palmeira (2007) reported that geotextiles have a superior blast-resistance performance to geogrids because soil particles can pass through the apertures of geogrids subjected to blast loads, which reduces their reinforcing effect. The geotextile selected in the present study is characterized by large plastic deformation, and its residual deformation could be preserved when the applied tensile load is released. The load-elongation behaviors of the geotextile were tested through wide-width (ASTM D4595) and biaxial tensile tests (Nguyen *et al.* 2013) in the longitudinal and transverse directions. A puncture tensile test (ASTM D6241) was conducted to evaluate the tensile behavior of the geotextile subjected to an axisymmetric compressive force pushing downward by a probe, similar to the effect of blast-induced pressure in the field. Detailed descriptions of the puncture tensile test are provided in Yang *et al.* (2016a). Figure 5 presents the photographs of the various tensile tests; Figure 6 presents the results of the tensile tests; and Table 3 summarizes the tensile properties of the geotextile. The results of the tensile tests indicate that the selected geotextile is an anisotropic tensile material. The tensile strength and stiffness of the geotextile in the longitudinal direction were higher than those in the transverse direction. Based on the results of the puncture tensile test, the geotextile had an ultimate tensile strength $T_{ult} = 12.3$ kN/m, and secant stiffness at a 50% stress level $J_{50} = 16.48$ kN/m.

After the explosion tests, the geotextile layers were retrieved from the test pit. Because these layers were unloaded, the measured residual tensile strain, which is representative of the plastic reinforcement deformation, was less than the mobilized tensile strain during the tests. Nguyen *et al.* (2013) proposed a technique for deriving the mobilized reinforcement tensile strain from the residual tensile strain. This technique was adopted in

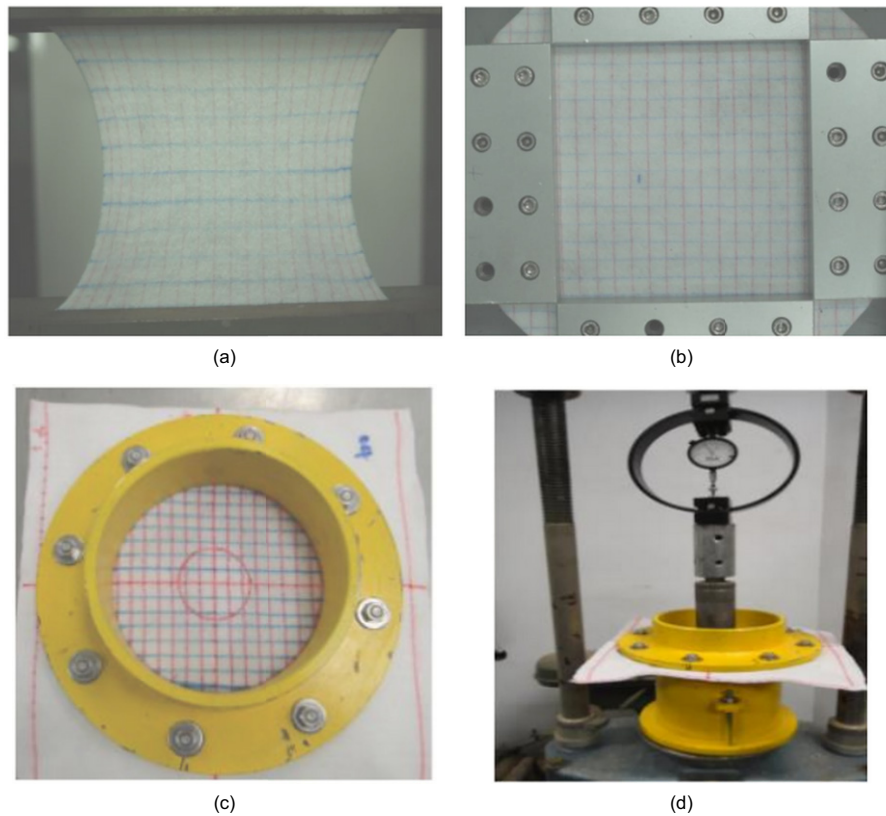


Figure 5. Photographs of reinforcement tensile tests: (a) wide-width tensile test; (b) biaxial tensile test; (c), (d) puncture tensile test

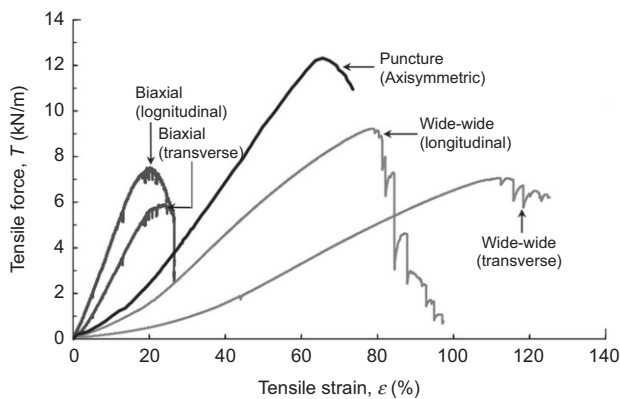


Figure 6. Load-strain response of nonwoven geotextile under various tensile test conditions

the present study to obtain the maximum reinforcement tensile strain developed during the explosion tests. The relationship between the mobilized and residual tensile strains was established through a series of tensile tests involving the initial loading of the reinforcement to several target tensile strain levels and the subsequent release of the tensile loads. The target tensile strains (controlled during the tests) and corresponding residual strains (obtained after releasing the load) were recorded and plotted. Figure 7 displays the relationship between the mobilized and residual tensile strains of the selected geotextile under various loading conditions. These strains had a unique relationship, irrespective of the loading condition. The intercept in Figure 7 indicates

Table 3. Properties of nonwoven geotextile

Tensile test	Ultimate tensile strength, T_{ult} (kN/m)	Failure strain, ϵ_f (%)	Secant stiffness at 50% stress level, J_{50} (kN/m)
Wide-width tensile test ^a	9.28/7.08	84.1/117.8	11.03/5.83
Biaxial tensile test ^a	7.53/5.91	20.3/24.3	37.09/24.32
Puncture tensile test ^b	12.3	65.6	16.48

^aTest results are asymmetric; values are presented in longitudinal/transverse directions.

^bTest results are axisymmetric.

that the geotextile remained elastic when the mobilized reinforcement tensile strain $\epsilon < 4\%$, and plastic deformation began to occur when $\epsilon \geq 4\%$.

2.3. Test preparation and procedure

Figure 8 presents the photographs of the explosion tests. The test pit was excavated, and the test model for reinforced soil was then constructed by placing a soil layer on the first (bottom) reinforcement layer. To achieve uniform density, the soil was backfilled in several lifts. The required weight of dry sand for each soil lift (= 5 cm) was calculated for $D_r = 40\%$, and the calculated quantity of sand was then carefully distributed in the test pit. The soil backfilled for loose conditions was to simulate an urgent construction process, which might be required during wartime. The geotextile layers were marked with blue grid lines, with

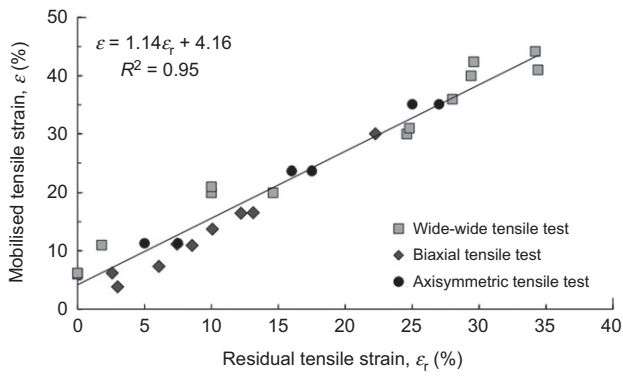


Figure 7. Relationships between mobilized and residual tensile strains under various loading conditions

2.5-cm line spacing in the transverse and longitudinal directions for facilitating the measurement of the change in the mobilized strain of the geotextile after the explosion tests. The marked geotextile was then laid over the sand layer, and the two ends of the geotextile layers in the longitudinal direction were wrapped around sandbags to provide anchorage against reinforcement pullout. The aforementioned construction processes were repeated thrice until the test model reached the ground level.

A total of 113 g of TNT was placed on top of the test models, and explosions were conducted twice for each test model. After the first blast, images of the blast-induced crater were taken, and the ground surface of the test model was backfilled and leveled. Subsequently, the second explosion was conducted. The blast pressures in air and soil, ground deformation, and mobilized reinforcement tensile strain

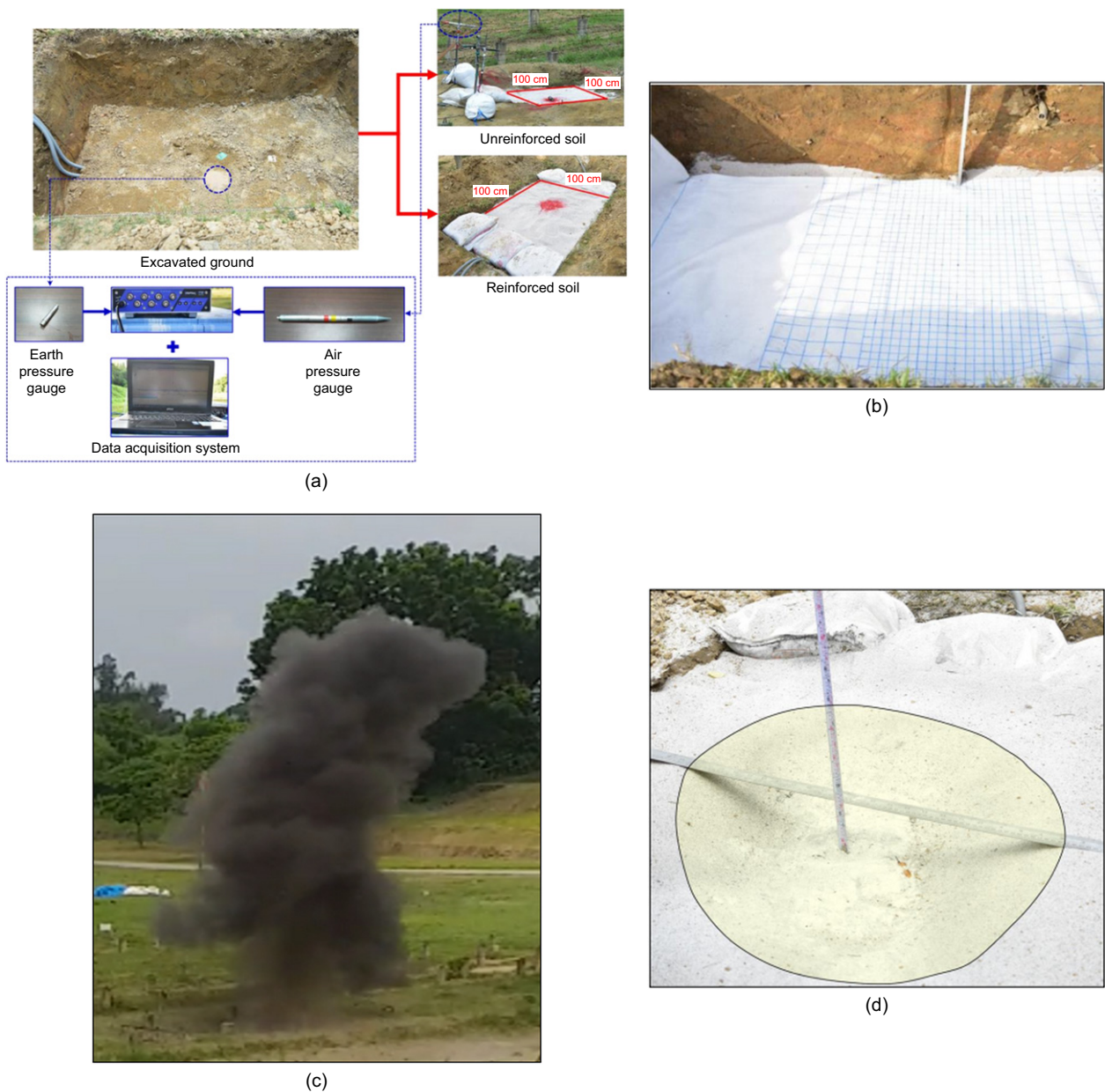


Figure 8. Photographs of the explosion test: (a) test pit and instrumentation arrangement; (b) installation of geotextile layers marked with blue grid lines; (c) TNT explosion and dust cloud; (d) blast-induced crater in the ground surface

were measured during the explosion tests. An earth pressure gauge (PCB 113B28) was installed at the bottom of the test pit ($R = 61$ cm) to measure the blast pressure produced in the soil. Three needle-shaped air pressure gauges (PCB 137A23) were attached to angle bars at various heights above the ground surface ($R = 100, 120,$ and 155 cm) to measure the blast pressure in air. The resolution of the pressure gauges was approximately ± 0.1 Pa, and the frequency of the recorded data reached a maximum value of 1×10^5 Hz. The measured pressure data were automatically transmitted to a data logger and then recorded by a computer. A charge-coupled device (CCD) camera was used to record the ground deformation caused by the explosions. The recorded photographic data were analyzed through digital image analysis techniques to obtain the sizes of the blast-induced craters. After the explosion tests were completed, each geotextile sheet was carefully retrieved from the dismantled model to determine the residual tensile deformation of the reinforcement. The measured reinforcement residual tensile strain ε_r was then converted into mobilized reinforcement tensile strain by using the following linear function (Figure 7): $\varepsilon = 1.14 \varepsilon_r + 4.16$.

3. TEST RESULTS

3.1. Blast pressure in air

Figure 9 illustrates the variations in the blast pressure in air with time at various distances from the explosive charge for the unreinforced soil. The measured blast pressure in air for the reinforced soil exhibited a similar trend to that of the unreinforced soil; therefore, the pressure in air for the reinforced soil is not shown repeatedly. Table 4 summarizes the peak blast pressure $P_{b,peak}$ in air at various distances from the explosive charge. As depicted in Figure 9, at a fixed location, soon after the explosion, the blast pressure increased steeply to a peak value (i.e. peak blast pressure or overpressure) because of the traveling of the blast wave and the arrival of a steep pressure front at this location. After the steep rise in the pressure, P_b quickly decreased to 0 (i.e. atmospheric pressure) and subsequently became negative because of the air suction created by the momentum of expanding gases. Finally, P_b returned to 0, and the entire explosion process was completed within a few milliseconds. The duration of the negative-pressure phase was generally longer than that of the positive-pressure phase. The observed pressure-time history was consistent with the law of propagation of explosions in air, which is described in the TM 5-855-1 and UFC 3-340-02 manuals of the US military.

For both the first and second explosions, the $P_{b,peak}$ value decreased, and the time required to reach the $P_{b,peak}$ value increased as the distance from the explosive charge increased (Figure 9). Table 4 presents a comparison of the measured $P_{b,peak}$ values with the peak incident pressure P_{so} and peak reflected pressure P_r values calculated using the design charts for a surface explosion presented in the UFC 3-340-02 manual. For the same distance from the explosive charge, the measured $P_{b,peak}$

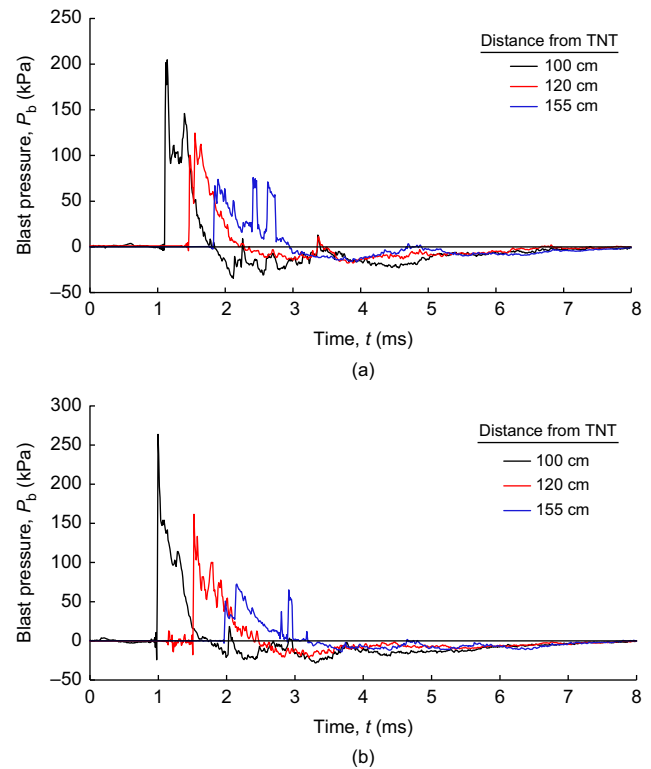


Figure 9. Time history of the blast pressures in air: (a) first blast; (b) second blast

Table 4. Summary of the peak blast pressures in air at various distances

Distance from TNT, R (cm)	U.S. military manual (UFC 3-340-02)		Measured peak blast pressure
	P_{so} (kPa)	P_r (kPa)	$P_{b,peak}$ (kPa)
100	165.1	521.5	204.8/263.6
120	111.2	316.0	124.6/161.6
155	65.8	165.6	73.9/72.6

Note: measured peak blast pressure values are presented for the first/second explosion.

values were close to the calculated P_{so} values and were considerably lower than the calculated P_r values, indicating that the measured $P_{b,peak}$ values mainly consisted of the incident pressure and were only slightly influenced by the reflected pressure. The comparison results also demonstrated that the measured $P_{b,peak}$ values were within a reasonable range.

3.2. Blast pressure in soil

Figure 10 displays the variations in the blast pressure in soil with time for the unreinforced and reinforced soils at the bottom of the test pit. Table 5 summarizes the peak blast pressures in the soils. In Figure 10, two pressure peaks can be observed for the unreinforced soil. The first peak was caused by the incident blast wave, and the

second peak was caused by the reflected blast wave, which arrived at the monitored point slightly after the incident blast wave. After the pressure peak occurred, the blast pressure rapidly decreased because of the energy attenuation caused by the friction of the sand. The measured $P_{b,peak}$ value for the unreinforced soil was approximately 540 kPa, which is close to the peak incident pressure (500 kPa) calculated using the design charts for a surface explosion presented in the TM 5-855-1 manual. The measured $P_{b,peak}$ values for the reinforced soil were 48.9 and 151.9 kPa during the first and second explosions, respectively. The $P_{b,peak}$ value for the reinforced soil during the second explosion was higher than that during the first explosion, possibly because of the soil densification caused by the first blast load and further enhanced by the reinforcement. The transmission of blast waves in the soil become faster, and thus the energy attenuation

effect decreased in the second explosion. The aforementioned finding is in line with that of Nguyen *et al.* (2020), who conducted a series of compaction tests on the soil reinforced with nonwoven geotextile layers and found that the density of reinforced soil was enhanced because soil displacement under compaction forces was restrained by nonwoven geotextile layers. Under the same compaction energy, the $\gamma_{d,max}$ of reinforced soil was 4.5–5.3% higher than that of unreinforced soil.

The most crucial finding obtained from Figure 10 is that the measured $P_{b,peak}$ values for the reinforced soil were substantially lower than those for the unreinforced soil. The $P_{b,peak}$ values in the reinforced soil were only 10% and 28% of those in the unreinforced soil in the first and second explosions, respectively. The soil reinforcement reduced the blast pressure through the tensioned membrane effect, which is discussed in Section 3.4. Moreover, the durations of the positive-pressure phase for the reinforced soil (approximately 4.2 ms in both explosions) were substantially longer than those for the unreinforced soil (approximately 0.46 ms in both explosions). The test results indicated that the inclusion of nonwoven geotextile in the soil modified the characteristics of the blast wave by decreasing the peak blast pressure and increasing the duration of the positive-pressure phase. The decrease in the peak blast pressure resulted in a decrease in the blast-induced load on the underground structure. Moreover, the increase in the duration of the blast wave resulted in a change in the nature of the blast load from a dynamic load to a quasi-static load, which reduced the harmful dynamic effects of the blast wave (Venkataramana *et al.* 2017). Based on the above discussion, the test results demonstrated that soil reinforcement is a valid mitigation measure against blast loads.

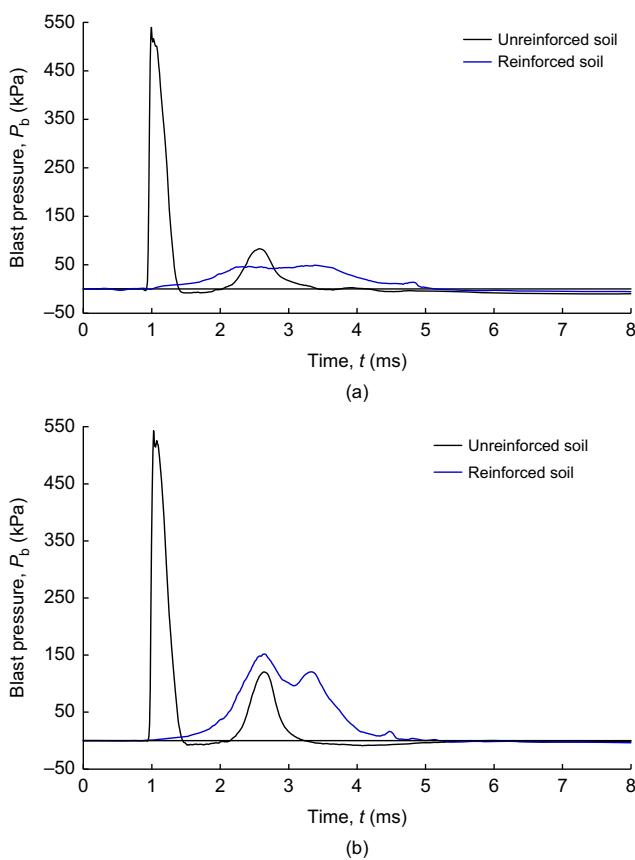


Figure 10. Time history of blast pressures in soil: (a) first blast; (b) second blast

Table 5. Summary of the peak blast pressures in unreinforced and reinforced soils

Distance from TNT, R (cm)	U.S. military manual (TM 5-855-1), P_{so} (kPa)	Measured peak blast pressure, $P_{b,peak}$ (kPa)	
		Unreinforced	Reinforced
61	500	539.9/542.9	48.9/151.9

Note: measured peak blast pressure values are presented for the first/second explosion.

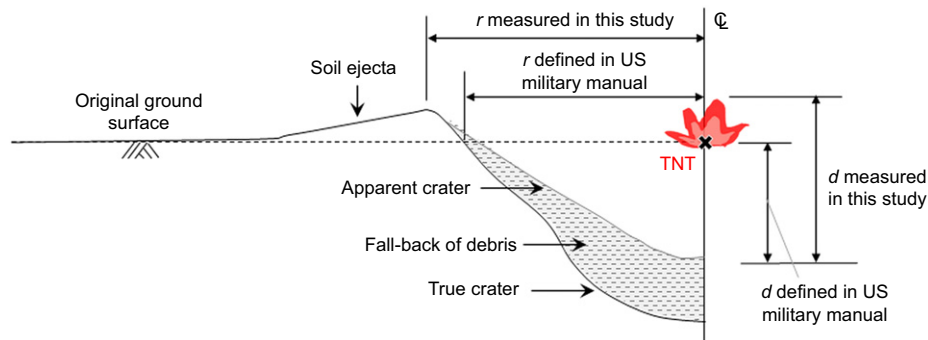
3.3. Ground and reinforcement deformation

Table 6 lists the depth, diameter, and volume of the blast-induced crater for the unreinforced and reinforced soils. After each explosion, images of the crater formed on the ground surface of the test pit were captured using the CCD camera, and the dimensions of the crater were measured (Figure 8a). The volume of the crater was then estimated using the equation for the volume of a half-ellipsoid. For comparison, Table 6 provides the dimensions of the crater calculated using the design charts for sandy soil in the TM 5-855-1 manual. The calculated crater depth matched the measured crater depth; however, the measured diameter was higher than the calculated diameter. This discrepancy resulted from the different reference elevations used for measuring the dimensions of the crater, as illustrated in Figure 11. In the TM 5-855-1 manual, the diameter of the apparent crater is defined at the elevation of the original ground surface. However, locating the original ground surface inside the crater is difficult in the field. In this study, the diameter of the crater was measured at the peak elevation of the soil ejecta; thus, the measured diameter was larger than the calculated one. Depending on the height and slope of the soil ejecta, the diameters

Table 6. Blast-induced ground deformation

U.S. military manual (TM 5-855-1), d & $2r$ (cm)	Measured depth and diameter of the crater, d & $2r$ (cm)		Estimated volume of the crater, $V = \frac{2}{3}\pi \times d \times r^2$ (cm ³)	
	Unreinforced	Reinforced	Unreinforced	Reinforced
12.1 & 45.9	12.2 & 75/15 & 85	10 & 70/10 & 75	35913/56716	25643/29437

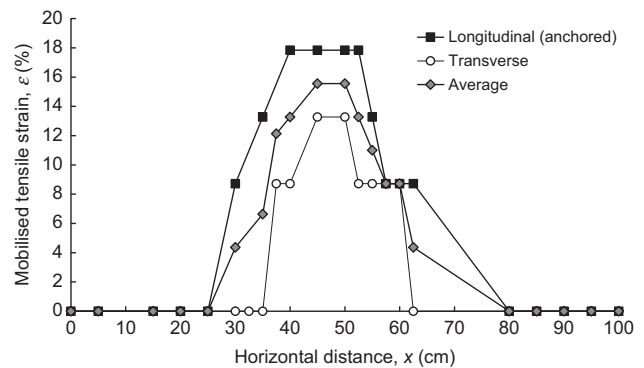
Note: measured peak blast pressure values are presented for the first/second explosion.

**Figure 11. Illustration of the dimensions of the crater**

measured at the aforementioned two elevations can differ by several centimeters.

The test results indicated the depth and diameter of the crater in the reinforced soil were lower than those of the crater in the unreinforced soil. Thus, the volume of the crater in the reinforced soil was on average 39% lower than that in the unreinforced soil, suggesting that the inclusion of nonwoven geotextile layers in soil can reduce the ground deformation caused by blast loads. The soil reinforcement reduced the ground deformation through the lateral restraint effect, which is discussed in the following section.

Figure 12 displays the mobilized tensile strain of the top reinforcement layer, which was estimated from its residual tensile strain. The distribution of the mobilized tensile strain of this layer was approximately symmetrical. It peaked at the center of the geotextile, aligned with the position of the explosive charge, and gradually decreased toward two ends. The maximum tensile strains were $\epsilon_{\max} = 18\%$ and 14% in the longitudinal and transverse directions, respectively. The length of mobilized tensile strain on the geotextile was approximately 55 cm (from $x = 25$ to 80 cm in Figure 12), suggesting the blast load was widely distributed by the geotextile. Careful inspection of the retrieved reinforcement layers after the explosion tests revealed that the geotextile remained intact and was not damaged by the blast. This finding can be justified by the fact that the maximum mobilized tensile strain of the reinforcement layer ($\epsilon_{\max} = 18\%$) was considerably less than the failure strain determined from the puncture tensile test ($\epsilon_f = 65.6\%$, as presented in Table 3). The second and third geotextile layers exhibited little residual strain after their retrieval from the dismantled soil model. The tensile strain developed during the explosion tests was likely less than 4% , which was within the range of elastic deformation (Figure 7); therefore, no residual strain was recorded after the explosion tests.

**Figure 12. Mobilized tensile strain of the top reinforcement layer**

3.4. Reinforcing mechanisms

On the basis of the results obtained in the explosion tests, two reinforcing mechanisms of reinforcement on mitigating blast loads were identified and illustrated in Figure 13. The first reinforcing mechanism was the tensioned membrane effect (Giroud *et al.* 1990). As a blast wave passed through the geotextile, the geotextile absorbed the blast load, which was distributed over a wide influence area. The vertical component of the mobilized tensile force also counterbalanced the blast pressure. Thus, the blast pressure reduced with depth as the blast wave propagated through the geotextile. Studies have reported the effectiveness of the tensioned membrane effect in supporting the overburden pressure and alleviating differential settlement for geosynthetic-reinforced piled embankments, reinforced foundations affected by fault movements, GRS integrated bridge systems, and GRS structures on yielding foundations (Han *et al.* 2007; Viswanadham and König 2009; Rajesh and Viswanadham 2012; Oettle and Bray 2013; Ohta *et al.* 2013; Miao *et al.* 2014; Chen *et al.* 2016; Talebi *et al.* 2017; Zheng and Fox 2017; Ardah *et al.* 2018; Sadat *et al.* 2018; King *et al.* 2019; Yang *et al.* 2020).

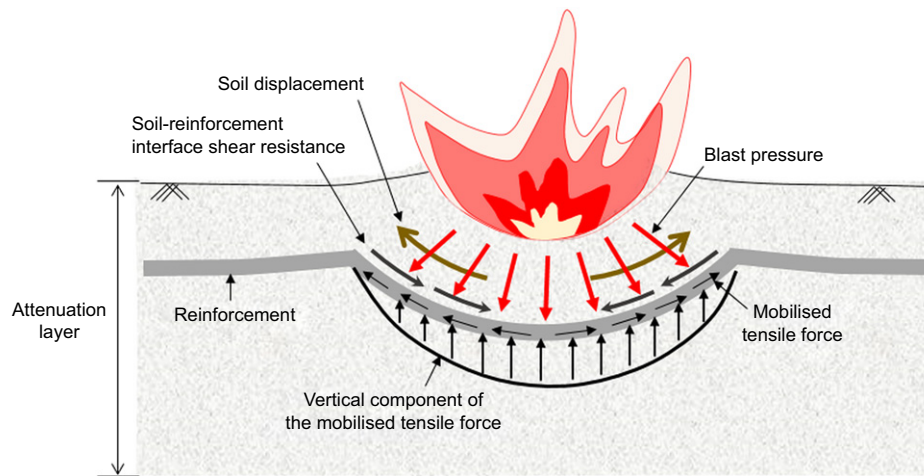


Figure 13. Illustration of reinforcing mechanism against blast load

The second reinforcing mechanism was the lateral restraint effect (Haliburton *et al.* 1981), under which soil displacement was restrained by the shear resistance of the soil–reinforcement interface, resulting in the formation of a small blast-induced crater. Studies have reported the effectiveness of the shear resistance of the soil–reinforcement interface in reducing displacement and increasing the shear strength of soil. Experimental studies on reduced- and full-scale reinforced soils have found that geotextile layers restrict the lateral expansion and vertical dilation of soil, which leads to an increase in the soil shear strength (Wu and Hong 2008, 2009; Nguyen *et al.* 2013, 2020; Wu *et al.* 2014). Studies on geosynthetic-stabilized subgrade soils have also demonstrated that the soil–reinforcement interaction can restrain soil deformation and thus reduce rutting depth and pavement cracks (Roodi and Zornberg 2017; Zornberg 2017; Zornberg *et al.* 2017; Sun *et al.* 2018; Sun and Han 2019a, 2019b).

4. NUMERICAL ANALYSIS AND VALIDATION

4.1. Numerical model and boundary conditions

Although field explosion tests are a direct method for assessing the effectiveness of reinforced soil against blast loads, these tests are difficult to conduct many times because they are labor-intensive, costly, and associated with safety concerns. Therefore, a series of numerical analyses were performed in this study to evaluate the effects of reinforcement parameters (i.e. number of reinforcement layers, ultimate tensile strength, and stiffness) on the blast pressure. These analyses were conducted using the LS-DYNA finite element program (LS-DYNA 2010) for nonlinear explicit dynamic computations. The arbitrary Lagrangian–Eulerian (ALE) algorithm was adopted for precisely simulating the fluid–structure interaction under large soil deformation, which is crucial for accurately modeling the behavior of air and soil under blast loading. LS-DYNA software has been widely adopted by researchers to simulate the effect of blast loads on air and soil (Wang 2001; Scherbatiuk and Rattanawangcharoen 2008; An *et al.* 2011; Cheng *et al.* 2013; De *et al.* 2016; Wang 2020, 2021).

Figure 14 shows the three-dimensional numerical model for simulating the field explosion test. The front face of the numerical model was considered to be symmetric in the vertical plane, so that simulations could be performed for only half the full model to decrease the computation time. The numerical model consisted of 1 40 864 eight-node hexahedral elements. The optimal mesh size of approximately 2 cm was determined based on a series of mesh sensitivity studies to balance the computational time and accuracy. All the faces of the numerical model, except for its front face, were set to have nonreflecting boundary conditions (NRBC); thus, pressure could flow out at these boundaries and did not cause reflection. The two ends of the geotextile layers in the longitudinal direction were fixed by hinges to mimic the reinforcement anchorage provided by the sandbags in the field. The soil–reinforcement interface was assumed to be fully bonded by using the `CONSTRAINED_LAGRANGE_IN_SOLID` command in the numerical model because reinforcement pullout was unlikely to occur due to the anchorage effect provided by the sandbags. Only the first explosion was simulated in the numerical analyses. The second explosion was not modeled because its modeling requires an advanced soil model that can consider the effect of the soil densification after the first blast.

4.2. Material model and input properties

Table 7 summarizes the material types, parameters, equations of states (EOSs), and input properties of the materials used in this study. TNT was modeled using `HIGH_EXPLOSIVE_BURN` material to simulate the behavior of an explosive. The pressure–volume–energy behavior caused by the chemical energy during the explosion was simulated using the Jones–Wilkins–Lee (JWL) EOS, which is expressed as follows:

$$P = A \left(1 - \frac{\omega}{R_1 V_r} \right) e^{-R_1 V_r} + B \left(1 - \frac{\omega}{R_2 V_r} \right) e^{-R_2 V_r} + \frac{\omega E_0}{V_r} \quad (2)$$

where P is the pressure per unit volume, A , B are the linear explosion coefficients, ω , R_1 , and R_2 are the nonlinear

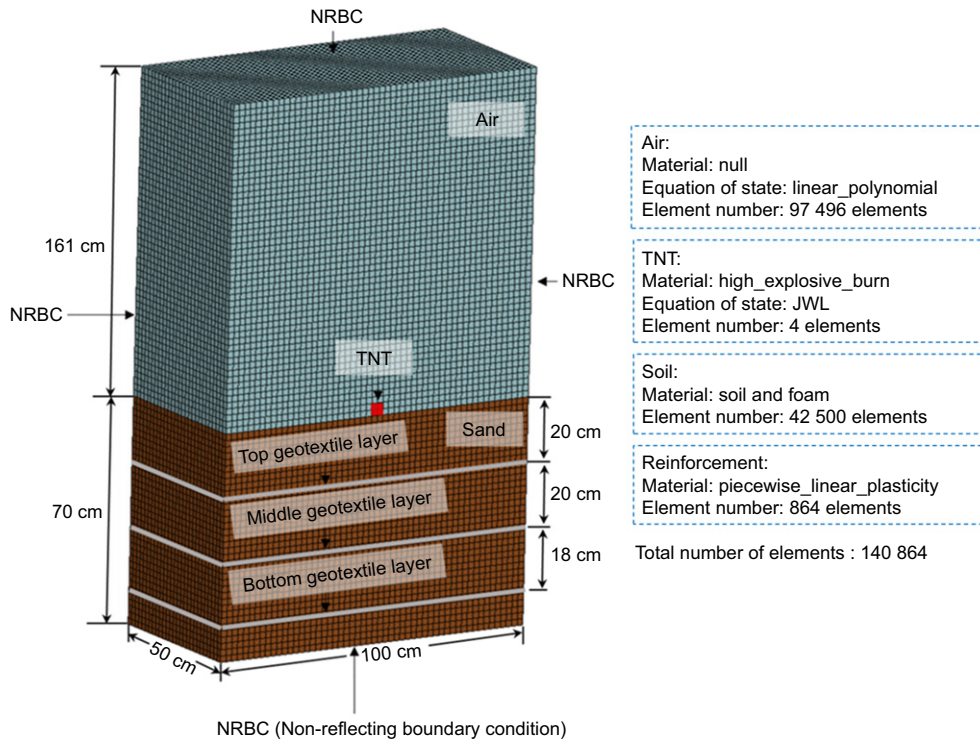


Figure 14. Numerical model for simulating explosion test

Table 7. Material parameters and input values

Material	Parameters and values
TNT	Material type 8: HIGH_EXPLOSIVE_BURN Mass density, ρ (kg/m ³) Detonation velocity, v_D (m/s) Chapman-Jouget pressure P_{CJ} (GPa) 1630 6930 21 Equation of State: JWL Coefficient A (GPa) Coefficient B (MPa) Coefficient R_1 Coefficient R_2 Coefficient ω 371 3.231 4.15 0.95 0.3 Initial energy, E_0 (J/m ³) Initial volume, V_0 (m ³) 6.99×10^9 1×10^{-6}
AIR	Material type 9: NULL Mass density, ρ (kg/m ³) Pressure cutoff, P_c (GPa) Viscosity coefficient, M_u 1.29 0 0 Equation of state: LINEAR_POLYNOMIAL Constant, C_0-C_3, C_6 Constant, C_4-C_5 Initial energy, E_0 (J/m ³) Initial volume, V_0 (m ³) 0 0.4 3.22×10^5 1×10^{-6}
SOIL	Material Type 5: SOIL_AND_FOAM Mass density, ρ (kg/m ³) Shear modulus, G (MPa) Bulk modulus, K (MPa) 1635 10 (top), 25 (middle), 40 (bottom) 525.4 Plastic yield function, a_0, a_1 Plastic yield function, a_2 0 0.567

explosion coefficients, V_r is the relative volume with respect to the initial volume, E_0 is the internal energy per unit volume, respectively. The input values for TNT (Table 7) were obtained from the Explosive Handbook by Dobratz (1981).

Air was modeled using NULL material, and the behavior of air was simulated using the LINEAR_POLYNOMIAL EOS. This EOS is expressed as follows:

$$P = C_0 + C_1\mu + C_2\mu^2 + C_3\mu^3 + (C_4 + C_5\mu + C_6\mu^2)E_0 \quad (3)$$

where P is the pressure per unit volume, E_0 is the initial internal energy per unit volume, and $\mu (= 1/V_r - 1)$ is the coefficient of dynamic viscosity. C_0-C_6 are the constant. The input values for air (Table 7) were obtained according to the Gamma law for ideal gases under atmospheric pressure.

Soil was modeled as an ALE multi-material solid element with SOIL_AND_FOAM material. The behavior of soil was simulated using the constitutive model of Krieg (1972). Krieg's model has been proven to be valid for simulating the dynamic response of sandy soils subjected to explosive compaction or surface explosion loading (Esmaili and Tavakoli 2019; Wang 2021). The input values for soil were calibrated from the experimental tests. The input soil density ($\rho = 1635 \text{ kg/m}^3$) corresponded to the field soil density in the explosion test. The bulk modulus K ($= 525.4 \text{ MPa}$) was determined from the initial consolidation phase of the consolidated-drained triaxial compression tests, as follows:

$$K = \frac{\sigma_m}{\varepsilon_v} \quad (4)$$

and

$$\sigma_m = \frac{\sigma_1 + \sigma_2 + \sigma_3}{3} \quad (5)$$

where σ_m is the mean stress, equal to the confining pressure applied at the initial consolidation phase, ε_v is the corresponding volumetric strain developed applied at the initial consolidation phase, σ_1 , σ_2 , and σ_3 are the principle stresses. The soil shear modulus varied from $G = 10.2$ to 41.4 MPa depending on the strain level (Figure 4). A preliminary numerical study was conducted to evaluate the strain level in the explosion test. The numerical results indicated that the soil strain caused by surface explosion decreased as the depth increased. The strain varied from approximately 1% at the ground surface to approximately $1 \times 10^{-3}\%$ at the bottom of the soil layers. Accordingly, the soil was divided into three layers (top, middle, and bottom soil layers; each with a thickness of 20 cm), and the input G value for a soil layer was selected according to the average strain level in the layer. In this study, $G = 10$, 25, and 40 MPa were selected for the top, middle, and bottom soil layers, respectively.

Krieg's yield criterion is based on isotropic plasticity theory, and the plastic yield function is expressed as follows:

$$f_p = J_2 - (a_0 + a_1 p + a_2 p^2) \quad (6)$$

where f_p is the plastic yield function, J_2 is the second invariant of the deviatoric stress tensor, p ($= \sigma_m$) is the mean stress, a_0 , a_1 , and a_2 are the constants of the yield function. The values of these constants can be estimated using the soil shear strength parameters as follows (Wang 2021):

$$a_0 = c'^2 \quad (7)$$

$$a_1 = 2c' \tan \phi' \quad (8)$$

$$a_2 = \tan^2 \phi' \quad (9)$$

From the triaxial tests, the values of c' and ϕ' were obtained as 0 kPa and 37° , respectively. By substituting the aforementioned values into Equations 7–9, a_0 , a_1 , and a_2 were obtained as 0, 0, and 0.567, respectively.

Reinforcement was modeled using a shell element with PIECEWISE_LINEAR_PLASTICITY material: the

reinforcement was considered to have linear elastic and perfectly plastic behavior. The thickness of the reinforcement in the numerical model was 2 mm. The input properties for reinforcement, including its density, secant modulus, and ultimate tensile strength, were obtained from the experimental tests, as described in Section 2.2.

4.3. Model validation

The numerical model was validated through a comparison of the predicted and measured results. Figure 15 presents a comparison of the measured and predicted blast pressures in air at $R = 100$ and 120 cm from the explosion source. Figure 16 displays a comparison of the predicted and measured peak blast pressures in air by various approaches. The predicted variations in the blast pressure in air generally matched well with the measured ones.

Figure 17 depicts a comparison of the measured and predicted blast pressures in the unreinforced and reinforced soils. The predicted blast pressure in the unreinforced soil was in good agreement with the measured blast pressure in the unreinforced soil for the two explosions. The predicted blast pressure in the reinforced soil was close to the measured blast pressure in the reinforced soil for the first blast; however, the predicted blast pressure in the reinforced soil was lower than the measured blast pressure in the reinforced soil for the second blast because the effect of soil densification was not considered in the numerical simulation.

Figure 18 presents a comparison of the measured and predicted mobilized reinforcement tensile strains.

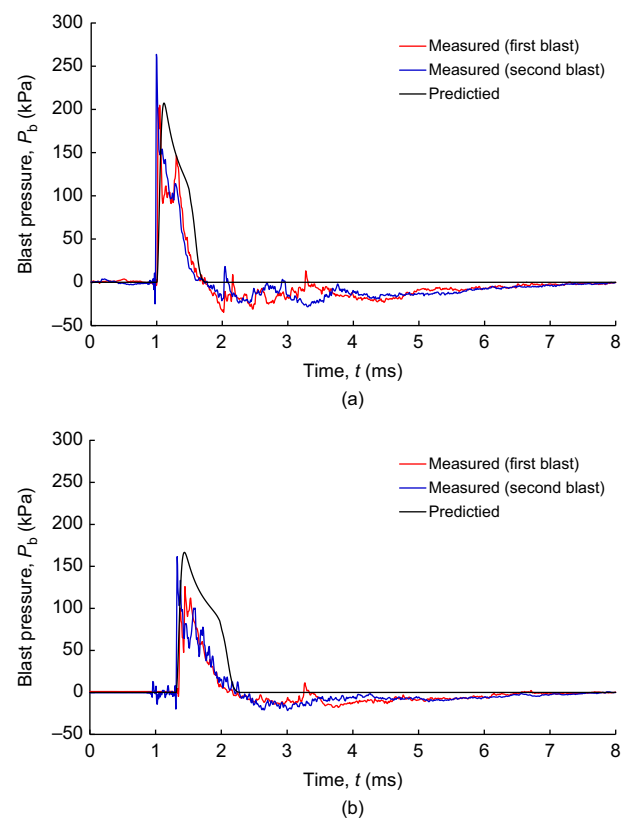


Figure 15. Comparison of the measured and predicted blast pressures in air: (a) $R = 100 \text{ cm}$; (b) $R = 120 \text{ cm}$

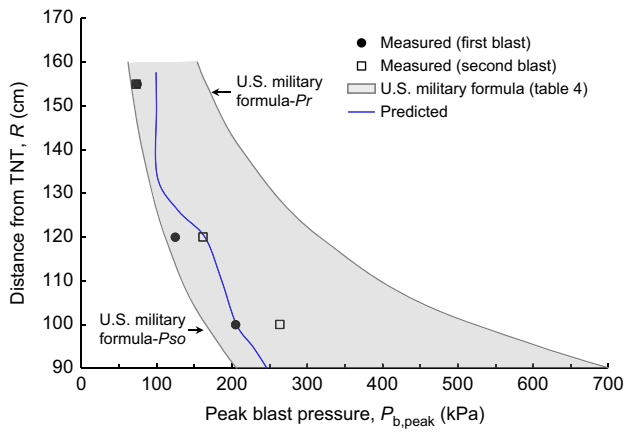


Figure 16. Comparison of the peak blast pressures in air by various approaches

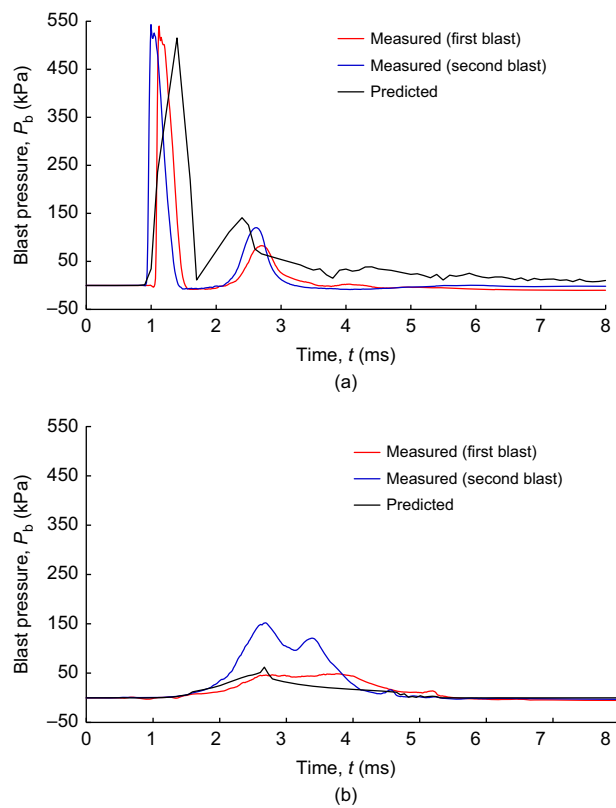


Figure 17. Comparison of the measured and predicted blast pressures in soil: (a) unreinforced soil; (b) reinforced soil

In general, the measured and predicted reinforcement tensile strains had similar distributions; however, the predicted ε_{\max} value ($\approx 13\%$) was marginally lower than the measured value ($= 15.5\%$). Three possible sources of error are discussed as follows. First, the actual reinforcement load–strain curve was nonlinear (Figure 6); the reinforcement stiffness in the puncture tensile test gradually increased as the mobilized tensile strain increased. Nevertheless, the reinforcement was modeled as a linear elastic–perfectly plastic material in the numerical analyses; the mean stiffness value (i.e. $J_{50} = 16.48$ kN/m in Table 3) was input as a representative value for the reinforcement. Because the input reinforcement stiffness

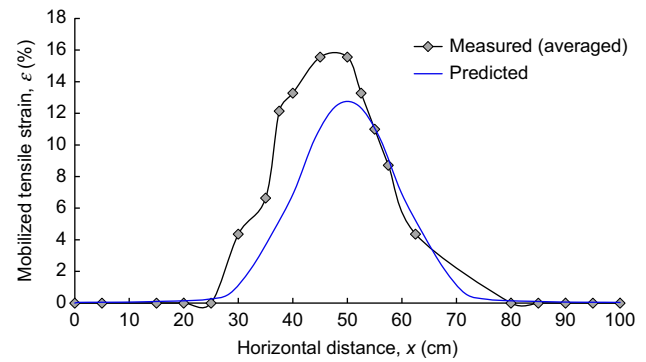


Figure 18. Comparison of measured and predicted mobilized reinforcement tensile strain

was higher than the actual stiffness under a low strain level, the ε_{\max} value was marginally underestimated in the numerical analyses. Second, the reinforcement load–strain response in the field explosion test was likely affected by the strain rate and soil confinement. Nonwoven geotextiles were found to be influenced by both strain rate and soil confinement (Boyle *et al.* 1996). The reinforcement in the field explosion test was subjected to rapid loading (strain rate $> 10^2$ s $^{-1}$) and in-soil conditions (with soil confinement); however, the reinforcement in the laboratory tensile tests was subjected to a relatively low strain rate ($= 10\%/min \approx 10^{-3}$ s $^{-1}$) and in-isolation conditions (without soil confinement). Therefore, the reinforcement tensile properties in the field explosion test could be different from those obtained from the laboratory tensile tests. Third, the measured ε_{\max} value in the field explosion test represented the strain accumulated from two blasts, whereas only one explosion was modelled in the numerical analyses.

After the numerical model was validated, the numerical results were examined to evaluate the influence of the tensioned membrane effect on the blast pressure in the soil. Figure 19 depicts a comparison of the blast pressure distributions in the unreinforced and reinforced soils at different depths when the peak blast pressure propagated through the top and bottom reinforcement layers. Figure 20 shows the propagation of the shock wave in terms of the change in the blast pressure contour in the reinforced soil. The numerical results indicated that the blast pressure considerably reduced with depth as the blast wave propagated through the geotextile layers. Notably, as depicted in Figure 20, when the shock wave contacted the top geotextile layer, a circular pressure contour was generated on the surface of the geotextile. This contour gradually expanded outward as the blast pressure propagated through the geotextile, indicating that the blast pressure was distributed over a wide influence area on the geotextile, which reduced the pressure transferred downward.

Another numerical analysis was performed using the validated model by increasing the depth of the unreinforced soil until $P_{b,\text{peak}}$ decreased to less than 62 kPa, which is equivalent to the $P_{b,\text{peak}}$ value at the bottom of the reinforced soil. The numerical results indicated that the aforementioned target $P_{b,\text{peak}}$ value was reached at a

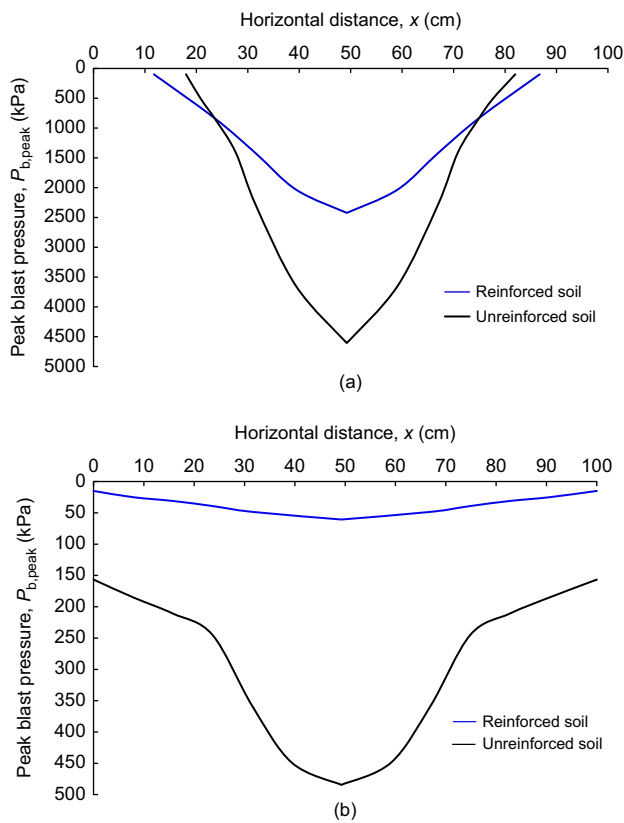


Figure 19. Distribution of blast pressures in soil at different depths when the peak blast pressure passed through: (a) the top layer ($D = 21$ cm); (b) the bottom layer ($D = 61$ cm)

depth of approximately of 180 cm in the unreinforced soil, which suggests that 60-cm-thick reinforced soil and 180-cm-thick unreinforced soil have equivalent effectiveness in reducing the blast pressure. This result also implies that the thickness of the attenuation layer can be considerably reduced using the reinforced soil; thus, soil reinforcement reduces the requirement of backfill materials and the overburden pressure acting on an underground structure.

4.4. Parametric study and sensitivity assessment

After model validation, a series of parametric studies were conducted to evaluate the effects of reinforcement parameters on the blast pressure. Table 8 presents the parametric study program. The variables considered in the parametric study were the number of reinforcement layers N , the reinforcement stiffness J_{50} , and the ultimate tensile strength T_{ult} . The numerical model used for model validation was also used in the parametric study, and the reinforcement properties used in model validation were referred to as the baseline case. For other simulations in the parametric study, only one target parameter varied each time, with the other parameters remaining unchanged. The influence of each parameter on the $P_{b,peak}$ value at the bottom of the soil layer was quantitatively compared.

Figure 21 gives the results of sensitivity assessment, which are presented as percentage changes in $P_{b,peak}$

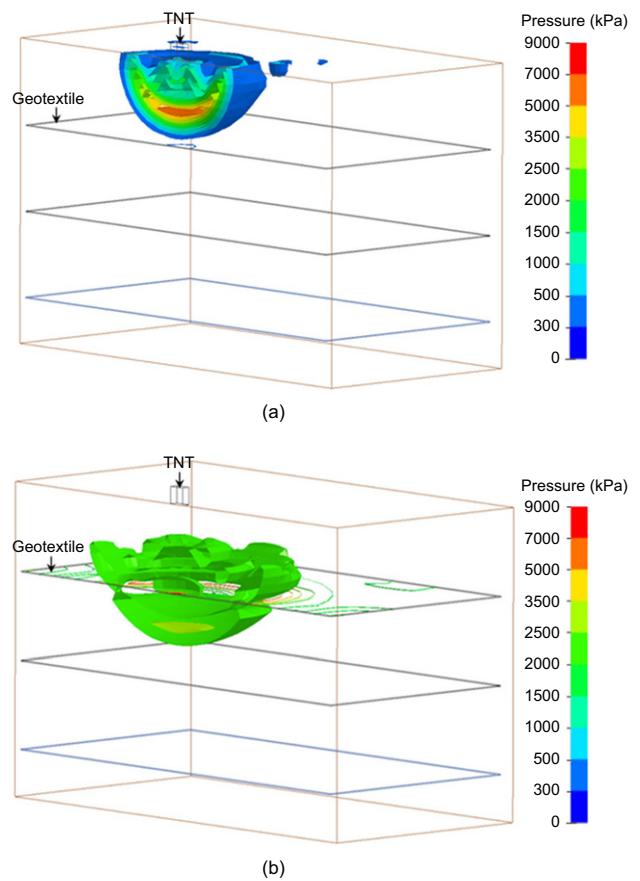


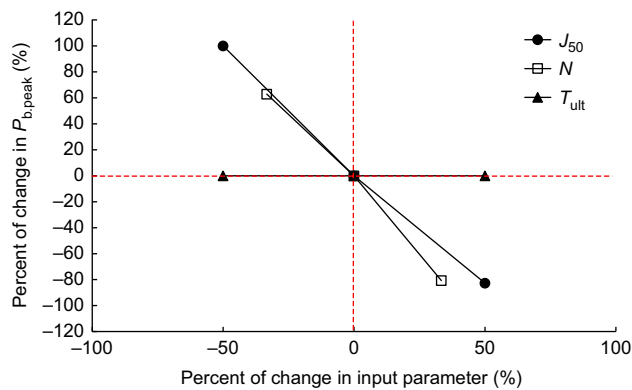
Figure 20. Propagation of the shock wave in term of the blast pressure contour in the reinforced soil: (a) before contacting the top geotextile layer; (b) contacting and passing through the top geotextile layer

versus percentage changes in input parameters. The percentage changes in input or output values were calculated in reference to the baseline case. The slope of each line in Figure 21 represents the degree of influence of an input parameter on $P_{b,peak}$. A line with a steep slope indicates that the input parameter has a strong influence on $P_{b,peak}$. The sensitivity assessment results indicated that N and J_{50} had a strong influence on $P_{b,peak}$. $P_{b,peak}$ values decreased by 80.6% and 82.7% when N increased by 33% and J_{50} increased by 50%, respectively. The aforementioned results were because a higher number of reinforcement layers or stiffer reinforcement can generate a stronger tensioned membrane effect, further reducing the $P_{b,peak}$ value. Yogendrakumar and Bathurst (1992) obtained similar findings in their numerical study. They found that GRS structures with higher reinforcement stiffness had better blast-resistance performance. Figure 21 also reveals that T_{ult} had a minor influence on the $P_{b,peak}$ value because the tensioned membrane effect (in terms of the mobilized reinforcement tension force) was unaffected by T_{ult} before the mobilized tensile force reached T_{ult} . However, if reinforcement breakage occurs ($T = T_{ult}$), the reinforcing effect can be substantially weakened because the reinforcement can no longer exert the tensioned membrane effect to reduce the blast pressure.

Table 8. Program and results of parametric study

Parameters	Reinforcement parameters			Results	
	Number of layer, N	Stiffness, J_{50} (kN/m)	Ultimate tensile strength, T_{ult} (kN/m)	Peak blast pressure at the bottom, $P_{b,peak}$ (kPa)	Percent of change in, $P_{b,peak}$ (%)
Baseline	3	16.48	12.3	62	0
Number of layers	2	16.48	12.3	101	+62.9
	4	16.48	12.3	12	-80.6
Stiffness	3	8.42	12.3	124	+100
	3	24.72	12.3	10.7	-82.7
Ultimate tensile strength	3	16.48	6.15	62	0
	3	16.48	18.45	62	0

Note: the percentage changes in input or output values are calculated in reference to the baseline case.

**Figure 21. Result of sensitivity assessment**

5. CONCLUSIONS

In this study, a series of experimental and numerical investigations were conducted to examine the performance and reinforcing mechanism of reinforced soil subjected to blast loads. The results of field explosion tests conducted in reinforced and unreinforced soil were compared to evaluate the effectiveness of soil reinforcement as a protective barrier against blast loads. Moreover, the effects of reinforcement parameters on the blast pressure were evaluated through a numerical parametric study. This study found that soil reinforcement is a valid mitigation measure against blast loads. The following conclusions were drawn:

- The pressure–time curve of the measured blast pressure in air was consistent with the law of propagation of explosions in air. As the distance from the explosive charge increased, the value of $P_{b,peak}$ and the time required to reach $P_{b,peak}$ increased. The measured $P_{b,peak}$ values were close to the P_{so} values calculated using the UFC 3-340-02 manual of the US military.
- The experimental results indicated that the inclusion of nonwoven geotextile in soil modified the characteristics of the blast wave in soil by decreasing the peak blast pressure and increasing the duration of the positive-pressure phase. The $P_{b,peak}$ values in the reinforced soil were only 10% and 28% of those in the unreinforced soil during the first and second explosions, respectively. The duration of the

- positive-pressure phase in the reinforced soil was nearly nine times higher than that in the unreinforced soil.
- Two reinforcing mechanisms of reinforcement on reducing blast loads were identified in this study. The first reinforcing mechanism was the tensioned membrane effect, under which geotextiles absorb blast loads and distribute them over a wide influence area. Moreover, the vertical component of the mobilized tensile force counterbalances the blast pressure. The second reinforcing mechanism was the lateral restraint effect, under which soil displacement is restrained by the shear resistance of the soil–reinforcement interface, which reduces the blast-induced ground deformation.
- The numerical analyses could satisfactorily predict the blast pressures in air and soil as well as the mobilized reinforcement tensile strain. The model validation results indicated that the numerical model developed in this study was appropriate for investigating the blast-resistance performance of unreinforced and reinforced soils subjected to surface explosion.
- The numerical results suggest that 60-cm-thick reinforced soil and 180-cm-thick unreinforced soil have equivalent effectiveness in blast pressure reduction, which implies that the thickness of the attenuation layer can be considerably reduced when using reinforced soil as a protective barrier against explosions.
- The results of the parametric study indicated that increases in the number of reinforcement layers and stiffness resulted in reductions in the $P_{b,peak}$ value. This phenomenon was observed because a higher number of reinforcement layers or stiffer reinforcement results in a stronger tensioned membrane effect. The ultimate tensile strength of the reinforcement had a minor influence on the $P_{b,peak}$ value before the mobilized tensile force reached T_{ult} .

The findings of this study are only applicable to the examined soil and reinforcement conditions and Hopkinson–Cranz scaled distance. The soil type, reinforcement type, and quantity of explosive charge might influence the blast-resistance performance of reinforced soil. These aspects require further investigation, so that an optimal

design can be developed for the attenuation layer used in soil reinforcement. Future studies could also investigate the effect of multiple explosions on the blast-resistance performance of reinforced soil.

ACKNOWLEDGEMENTS

This research was supported by the Ministry of Science and Technology, Taiwan under the grant number MOST110-2628-E-002-003. The authors also sincerely appreciate Military Academy, Taiwan for providing the experimental site for the explosion tests, National Defense University Army Command and Staff College, Taiwan for providing technical support, and Prowave Engineering Inc. for assisting with field instrumentation.

NOTATION

Basic SI units are given in parentheses.

A, B	linear explosion coefficients of JWL EOS (dimensionless)	V_r	relative volume with respect to the initial volume (dimensionless)
a_0, a_1, a_2	constants of the yield function (dimensionless)	v_d	detonation velocity (m/s)
C_0-C_6	constant of linear polynomial EOS (dimensionless)	W	weight of the explosive charge (g)
C_c	coefficient of curvature (dimensionless)	x	horizontal distance (m)
C_u	coefficient of uniformity (dimensionless)	Z_s	scaled distance (kg/m^3)
c'	cohesion (N/m^2)	γ	soil unit weight (N/m^3)
D_{10}, D_{60}	particle size corresponding to 10% and 60% finer (m)	$\gamma_{d,\max}$	maximum dry unit weight (N/m^3)
D_{50}	mean particle size (m)	$\gamma_{d,\min}$	minimum dry unit weight (N/m^3)
D_r	relative density (dimensionless)	ε	tensile strain (dimensionless)
d	diameter of the blast-induced crater (m)	ε_{DA}	double amplitude strain (dimensionless)
E_0	internal energy per unit volume (J/m^3)	ε_f	failure strain (dimensionless)
G	shear modulus (N/m^2)	ε_{\max}	maximum tensile strain (dimensionless)
G_s	specific gravity (dimensionless)	ε_r	residual tensile strain (dimensionless)
J_2	second invariant of the deviatoric stress tensor (N^2/m^4)	ε_v	volumetric strain (dimensionless)
J_{50}	secant stiffness at a 50% stress level (N/m)	μ	coefficient of dynamic viscosity (dimensionless)
K	bulk modulus (N/m^2)	ρ	mass density (kg/m^3)
N	number of reinforcement layers (dimensionless)	$\sigma_1, \sigma_2, \sigma_3$	principle stress (N/m^2)
P	pressure per unit volume (N/m)	σ_m	mean stress (N/m^2)
P_b	blast pressure (N/m^2)	ϕ'	friction angle ($^\circ$)
$P_{b,\text{peak}}$	peak blast pressure (N/m^2)	ω	nonlinear explosion coefficients of JWL EOS (dimensionless)
P_{CJ}	Chapman-Jouget pressure (N/m^2)		
P_r	peak reflected pressure (N/m^2)		
P_{so}	peak incident pressure (N/m^2)		
p	mean stress ($= \sigma_m$) (dimensionless)		
R	distance from the center of the explosive charge to the target (m)		
R_1, R_2	nonlinear explosion coefficients of JWL EOS (dimensionless)		
r	radius of the blast-induced crater (m)		
T_{ult}	ultimate tensile strength (N/m)		
t	time (s)		
V	volume of the blast-induced crater (m^3)		
V_0	initial volume (m^3)		

ABBREVIATIONS

ALE	arbitrary Lagrangian–Eulerian
ASTM	American society for Testing and Materials
CCD	charge-coupled device
EOS	equations of states
JWL	Jones–Wilkins–Lee
NRBC	non-reflecting boundary condition
SP	poorly graded sand
TNT	trinitrotoluene
USCS	Unified Soil Classification System

REFERENCES

- AbdelSalam, S. S. & Azzam, S. A. (2016). Reduction of lateral pressures on retaining walls using geofabric inclusion. *Geosynthetics International*, **23**, No. 6, 395–407.
- Anil, O., Erdem, R. T. & Kantar, E. (2015). Improving the impact behaviour of pipes using geofabric layer for protection. *International Journal of Pressure Vessels and Piping*, **132–133**, 52–64.
- An, J., Tuan, C. Y., Cheeseman, B. A. & Gazonas, G. A. (2011). Simulation of soil behavior under blast loading. *International Journal of Geomechanics*, **11**, No. 4, 323–334.
- Ardah, A., Abu-Farsakh, M. Y. & Voyiadjis, G. Z. (2018). Numerical evaluation of the effect of differential settlement on the performance of GRS-IBS. *Geosynthetics International*, **25**, No. 4, 427–441.
- ASTM D3999. Standard test method for the determination of the modulus and damping properties of soil using the cyclic triaxial apparatus. ASTM International, West Conshohocken, PA, USA.
- ASTM D4595. Standard test method for tensile properties of geotextiles by the wide-width strip method. ASTM International, West Conshohocken, PA, USA.
- ASTM D6241. Standard test method for geotextile puncture testing. ASTM International, West Conshohocken, PA, USA.
- Babagiray, G., Akbaş, S. O. & Anil, O. (2016). Investigation of impact behavior of HDPE pipes with geocell protective layer. *6th European Geosynthetics Congress (EuroGeo6)*, International Geosynthetics Society, Ljubljana, Slovenia, pp. 762–773.

- Baker, W. E., Westine, P. S. & Dodge, F. T. (1973). *Similarity Methods in Engineering Dynamics*. Spartan Books, Rochelle Park, NJ, USA.
- Baziar, M. H., Shahnazari, H. & Kazemi, M. (2018). Mitigation of surface impact loading effects on the underground structures with geofoam barrier: centrifuge modeling. *Tunnelling and Underground Space Technology*, **80**, 128–142.
- Boyle, S. R., Gallagher, M. & Holtz, R. D. (1996). Influence of strain rate, specimen length and confinement on measured geotextile properties. *Geosynthetics International*, **3**, No. 2, 205–225.
- Brandl, H. (2011). Geosynthetics applications for the mitigation of natural disasters and for environmental protection. *Geosynthetics International*, **18**, No. 6, 340–390.
- Chen, J. F., Tolooiyan, A., Xue, J. F. & Shi, Z. M. (2016). Performance of a geogrid reinforced soil wall on PVD drained multilayer soft soils. *Geotextiles and Geomembranes*, **44**, No. 3, 219–229.
- Cheng, D. S., Hong, C. W. & Pi, S. J. (2013). Numerical simulation of near-field explosion. *Journal of Applied Science and Engineering*, **16**, No. 1, 61–67.
- Choudhury, D. & Ahmad, S. M. (2007). Design of waterfront retaining wall for the passive case under earthquake and tsunami. *Applied Ocean Research*, **29**, No. 1–2, 37–44.
- Cuomo, S., Moretti, S., Wang, Y., D'Amico, A., Frigo, L. & Aversa, S. (2020). Modelling of geosynthetic-reinforced barriers under dynamic impact of debris avalanche. *Geosynthetics International*, **27**, No. 1, 65–78.
- Dave, M. M. & Solanki, C. H. (2020). Protection of buried pipelines using geosynthetics under different loading conditions—a review. *Advances in Computer Methods and Geomechanics. Lecture Notes in Civil Engineering*, **55**, 249–262.
- De, A. & Zimmie, T. F. (2016). Effects of surface explosion on underground tunnel and potential mitigation measures. *Transportation Infrastructure Geotechnology*, **3**, No. 2, 74–90.
- De, A., Morgante, A. N. & Zimmie, T. F. (2016). Numerical and physical modeling of geofoam barriers against effects of surface blast on underground tunnels. *Geotextiles and Geomembranes*, **44**, No. 1, 1–12.
- Dobratz, B. M. (1981). *LLLNL Explosives Handbook: Properties of Chemical Explosives and Explosive Simulants*. UCRL-52997, Lawrence Livermore National Laboratory, Livermore, CA, USA.
- Esmaili, M. & Tavakoli, B. (2019). Finite element method simulation of explosive compaction in saturated loose sandy soils. *Soil Dynamics and Earthquake Engineering*, **116**, 446–459.
- Fattah, M. Y. & Redha, W. B. M. (2016). Effect of geocell reinforcement in the mitigation of traffic loads transmitted to the flexible buried pipes. *Global Journal of Engineering Science and Research Management*, **3**, No. 7, 118–128.
- Fowze, J. S. M., Bergado, D. T., Soelump, S., Voottipreux, P. & Dechaskulsom, M. (2012). Rain-triggered landslide hazards and mitigation measures in Thailand: from research to practice. *Geotextiles and Geomembranes*, **30**, 50–64.
- Giroud, J. P., Bonaparte, R., Beech, J. & Gross, B. (1990). Design of soil layer-geosynthetic systems overlying voids. *Geotextiles and Geomembranes*, **9**, No. 1, 11–50.
- Haliburton, T., Lawmaster, J. & McGuffey, V. (1981). *Use of Engineering Fabrics in Transportation Related Applications*, FHWA DTFH61-80-C-00094. Federal Highway Administration, Washington, DC, USA.
- Han, J., Oztoprak, S., Parsons, R. L. & Huang, J. (2007). Numerical analysis of foundation columns to support widening of embankments. *Computer and Geotechnics*, **34**, No. 6, 435–448.
- Hegde, A. M. & Sitharam, T. G. (2015). Experimental and numerical studies on protection of buried pipelines and underground utilities using geocells. *Geotextiles and Geomembranes*, **43**, No. 5, 372–381.
- Khodaparast, M., Mohamad Momeni, R. & Bayesteh, H. (2022). Numerical simulation of surface blast reduction using composite backfill. *Geosynthetics International*, **29**, No. 1, 66–80.
- Kim, K.-M., Briaud, J.-L., Bligh, R. & Abu-Odeh, A. (2010). Full-scale impact test of four traffic barriers on top of an instrumented MSE wall. *Journal of Geotechnical and Geoenvironmental Engineering*, **136**, No. 3, 431–438.
- King, L., Bouazza, A., Gaudin, C., O'Loughlin, C. D. & Bui, H. H. (2019). Behavior of geosynthetic-reinforced piled embankments with defective piles. *Journal of Geotechnical and Geoenvironmental Engineering*, **145**, No. 11, 04019090.
- Koseki, J. & Shibuya, S. (2014). Mitigation of disasters by earthquakes, tsunamis, and rains by means of Geosynthetic-reinforced soil retaining walls and embankments. *Transportation Infrastructure Geotechnology*, **2**, No. 1, 231–261.
- Krieg, R. D. (1972). *A Simple Constitutive Description for Cellular Concrete*, SC-DR-72-0883. Sandia National Laboratories, Albuquerque, NM, USA.
- Kuwano, J., Miyata, Y. & Koseki, J. (2012). Performance of reinforced soil walls during the 2011 Tohoku earthquake. *Geosynthetics International*, **21**, No. 3, 179–196.
- Lambert, S. & Bourrier, F. (2013). Design of rockfall protection embankments: a review. *Engineering Geology*, **154**, 77–88.
- Lambert, S., Gotteland, P. & Nicot, F. (2009). Experimental study of the impact response of geocells as components of rockfall protection embankments. *Natural Hazards and Earth System Sciences*, **9**, No. 2, 459–467.
- Liu, C. N., Huang, W. W., Lin, B. H. & Ho, Y. H. (2021). Finite element analyses of geosynthetic-reinforced soil ground under surcharge and probabilistic estimation of the bearing capacity. *Journal of GeoEngineering*, **16**, No. 3, 99–109.
- LS-DYNA (2010). *LS-DYNA User's Manual*. Livermore Software Technology Corporation, Livermore, CA, USA.
- Martínez-Hergueta, F., Ridruejo, A., González, C. & Llorca, J. (2017). Numerical simulation of the ballistic response of needle-punched nonwoven fabrics. *International Journal of Solids and Structures*, **106–107**, 56–67.
- Martínez-Hergueta, F., Ridruejo, A., González, C. & Llorca, J. (2022). Ballistic response of needle-punched nonwovens. *Mechanics of Fibrous Networks*, pp. 241–261.
- Miao, L., Wang, F., Han, J. & Lv, W. (2014). Benefits of geosynthetic reinforcement in widening of embankments subjected to foundation differential settlement. *Geosynthetics International*, **21**, No. 5, 321–332.
- Ng, C. C., Chew, S. H., Karunaratne, G. P., Tan, S. A. & Loh, S. L. (2000). Flexible and rigid faced MSE walls subject to blasting. *Advances in Transportation and Geoenvironmental Systems Using Geosynthetics*, ASCE, Reston, VA, USA, pp. 322–336.
- Nguyen, M. D., Yang, K. H., Lee, S. H., Wu, C. S. & Tsai, M. H. (2013). Behavior of nonwoven-geotextile-reinforced sand and mobilization of reinforcement strain under triaxial compression. *Geosynthetics International*, **20**, No. 3, 207–225.
- Nguyen, M. D., Yang, K. H. & Yalaw, W. M. (2020). Compaction behavior of nonwoven geotextile-reinforced clay. *Geosynthetics International*, **27**, No. 1, 16–33.
- Oettle, N. K. & Bray, J. D. (2013). Geotechnical mitigation strategies for earthquake surface fault rupture. *Journal of Geotechnical and Geoenvironmental Engineering*, **139**, No. 11, 1864–1873.
- Ohta, H., Ishigaki, T. & Tatta, N. (2013). Retrofit technique for asphalt concrete pavements after seismic damage. *Proceedings of 18th International Conference on Soil Mechanics and Geotechnical Engineering*, Paris, France, pp. 1333–1336.
- Ossa, A. & Romo, M. P. (2009). Micro- and macro-mechanical study of compressive behavior of expanded polystyrene geofoam. *Geosynthetics International*, **16**, No. 5, 327–338.
- Palmeira, E. M. & Andrade, H. K. P. A. (2010). Protection of buried pipes against accidental damage using geosynthetics. *Geosynthetics International*, **17**, No. 4, 228–241.
- Peila, D., Oggeri, C. & Castiglia, C. (2007). Ground reinforced embankments for rockfall protection: design and evaluation of full scale tests. *Landslides*, **4**, No. 3, 255–265.
- Pieri, R. (1998). *Using Reinforced Earth Walls for Blast Mitigation*. Master's Thesis, Department of Civil Engineering, University of Florida, Gainesville, FL, USA.
- Pires, A. C. G. & Palmeira, E. M. (2021). The influence of geosynthetic reinforcement on the mechanical behaviour of soil-pipe systems. *Geotextiles and Geomembranes*, **49**, No. 5, 1117–1128.
- Rajesh, S. & Viswanadham, B. V. S. (2012). Centrifuge modeling and instrumentation of geogrid-reinforced soil barriers of landfill

- covers. *Journal of Geotechnical and Geoenvironmental Engineering*, **138**, No. 1, 26–37.
- Recio-Molina, J. & Yasuhara, K. (2005). Stability of modified geotextile wrap around revetments for coastal protection. *Geosynthetics International*, **12**, No. 5, 260–268.
- Ronco, C., Oggeri, C. & Peila, D. (2009). Design of reinforced ground embankments used for rockfall protection. *Natural Hazards and Earth System Sciences*, **9**, 1189–1199.
- Roodi, G. H. & Zornberg, J. G. (2017). Stiffness of soil-geosynthetic composite under small displacements. II: experimental evaluation. *Journal of Geotechnical and Geoenvironmental Engineering*, **143**, No. 10, 04017076.
- Sadat, R. S., Huang, J., Bin-Shafique, S. & Rezaeimalek, S. (2018). Study of the behavior of mechanically stabilized earth (MSE) walls subjected to differential settlements. *Geotextiles and Geomembranes*, **46**, No. 1, 77–90.
- Scherbatiuk, K. & Rattanawangcharoen, N. (2008). Experimental testing and numerical modeling of soil-filled concertainer walls. *Engineering Structures*, **30**, No. 12, 3545–3554.
- Soude, M., Chevalier, B., Grediac, M., Talon, A. & Gourves, R. (2013). Experimental and numerical investigation of the response of geocell reinforced walls to horizontal localized impact. *Geotextiles and Geomembranes*, **39**, 39–50.
- Sun, X. & Han, J. (2019a). Mechanistic-empirical analysis of geogrid-stabilized layered system: part I. Solution development. *Geosynthetics International*, **26**, No. 3, 273–285.
- Sun, X. & Han, J. (2019b). Mechanistic-empirical analysis of geogrid-stabilized layered system: part II. Solution verification and discussion. *Geosynthetics International*, **26**, No. 3, 286–296.
- Sun, X., Han, J., Parsons, R. L. & Thakur, J. (2018). Equivalent California bearing ratios of multi-axial geogrid-stabilized aggregates over weak subgrade. *Journal of Materials in Civil Engineering*, **30**, No. 11, 04018284.
- Talebi, M., Meehan, C. L. & Leshchinsky, D. (2017). Applied bearing pressure beneath a reinforced soil foundation used in a geosynthetic reinforced soil integrated bridge system. *Geotextiles and Geomembranes*, **45**, No. 6, 580–591.
- Tuan, C. (2014). Ground shock resistance of mechanically stabilized earth walls. *International Journal of Geomechanics*, **14**, No. 3, 06014003.
- Tupa, N. & Palmeira, E. M. (2007). Geosynthetic reinforcement for the reduction of the effects of explosions of internally pressurised buried pipes. *Geotextiles and Geomembranes*, **25**, No. 2, 109–127.
- USDA (United States Department of the Army) (1998). *Army Technical Manual No. TM 5-855-1: Design and Analysis of Hardened Structures to Convention Weapon Effects*. Headquarters Departments of the Army, the Air Force, the Navy and the Defense Special Weapons Agency, Washington, DC, USA.
- USDA (2008). *Unified Facilities Criteria No. UFC 3-340-02: Structures to Resist the Effects of Accidental Explosions*. Department of the Army and Defense Special Weapons Agency, Washington, DC, USA.
- Venkataramana, K., Singh, R. K., Deb, A., Bhasin, V., Vaze, K. K. & Kushwaha, H. S. (2017). Blast protection of infrastructure with fluid filled cellular polymer foam. *Procedia Engineering*, **173**, 547–554.
- Vivek, P. & Sitharam, T. G. (2017). Shock wave attenuation by geotextile encapsulated sand barrier systems. *Geotextiles and Geomembranes*, **45**, No. 3, 149–160.
- Viswanadham, B. V. S. & Konig, D. (2009). Centrifuge modeling of geotextile-reinforced slopes subjected to differential settlements. *Geotextiles and Geomembranes*, **27**, No. 2, 77–88.
- Wang, J. (2001). *Simulation of Landmine Explosion Using LS-DYNA 3D Software: Benchmark Work of Simulation of Explosion in Soil and Air*. DSTO Aeronautical and Maritime Research Laboratory, Australia, DSTO-TR-1168.
- Wang, I. T. (2020). Nonlinear dynamic response and deformation analysis of soil under the explosion shock loading. *Journal of Vibroengineering*, **22**, No. 7, 1648–1660.
- Wang, I. T. (2021). Numerical and experimental approach for failure analysis of soil subjected to surface explosion loading. *Shock and Vibration*, **2021**, No. 1, 4981507.
- Wang, Z. L., Li, Y. C. & Wang, J. G. (2006). Numerical analysis of attenuation effect of EPS geofoam on stress-waves in civil defense engineering. *Geotextiles and Geomembranes*, **24**, No. 5, 265–273.
- Wang, L., Liu, S., Shen, C. & Lu, Y. (2021). Laboratory test and modelling of gas pressure under geomembranes subjected to the rise of groundwater in plain reservoirs. *Geotextiles and Geomembranes*, **49**, No. 1, 81–96.
- Watanabe, K., Nakajima, S., Fujii, K., Matsuura, K., Kudo, A., Nonaka, T. & Aoyagi, Y. (2020). Development of geosynthetic-reinforced soil embankment resistance to severe earthquakes and prolonged overflows due to tsunamis. *Soils and Foundations*, **60**, No. 6, 1371–1386.
- Witthoef, A. F. & Kim, H. (2016). Numerical investigation of earth pressure reduction on buried pipes using EPS geofoam compressible inclusions. *Geosynthetics International*, **23**, No. 4, 677–693.
- Woods, R. D. & Jedelet, L. P. (1985). Energy attenuation relationships from construction vibrations. *Vibration Problems in Geotechnical Engineering*, ASCE, New York, NY, USA, pp. 229–246.
- Wu, C. S. & Hong, Y. S. (2008). The behavior of a laminated reinforced granular column. *Geotextiles and Geomembranes*, **26**, No. 4, 302–316.
- Wu, C. S. & Hong, Y. S. (2009). Laboratory tests on geosynthetic-encapsulated sand columns. *Geotextiles and Geomembranes*, **27**, No. 2, 107–120.
- Wu, J. T. H., Yang, K.-H., Mohamed, S., Pham, T. & Chen, R.-H. (2014). Suppressing dilation of soil-a reinforcing mechanism of soil-geosynthetic composites. *Transportation Infrastructure Geotechnology*, **1**, No. 1, 68–82.
- Xu, F., Li, W. L., Liu, Z. L., Zhang, B. F. & Zhang, B. Y. (2017). Study of factors that influence geomembrane air expansion deformation under ring-restrained conditions. *Geotextiles and Geomembranes*, **45**, No. 3, 178–183.
- Yang, K.-H., Yalaw, W. M. & Nguyen, M. D. (2016a). Behavior of geotextile-reinforced clay with a coarse material sandwich technique under unconsolidated-undrained triaxial compression. *International Journal of Geomechanics, ASCE*, **16**, No. 3, 04015083.
- Yang, K. H., Wu, J. T. H., Chen, R. H. & Chen, Y. S. (2016b). Lateral bearing capacity and failure mode of geosynthetic-reinforced soil barriers subject to lateral loadings. *Geotextiles and Geomembranes*, **44**, No. 6, 799–812.
- Yang, K. H., Chiang, J., Lai, C. W., Han, J. & Lin, M. L. (2020). Performance of geosynthetic-reinforced soil foundations across a normal fault. *Geotextiles and Geomembranes*, **48**, No. 3, 357–373.
- Yasuhara, K. & Recio-Molina, J. (2007). Geosynthetic-wrap around revetments for shore protection. *Geotextiles and Geomembranes*, **25**, No. 4–5, 221–232.
- Yogendrakumar, M. & Bathurst, R. J. (1992). Numerical simulation of reinforced soil structures during blast loads. *Transportation Research Record*, **1336**, 1–8.
- Zhao, P., Yuan, S., Li, L., Ge, Q., Liu, J. & Du, L. (2021). Experimental study on the multi-impact resistance of a composite cushion composed of sand and geofoam. *Geotextiles and Geomembranes*, **49**, No. 1, 45–56.
- Zheng, Y. & Fox, P. J. (2017). Numerical investigation of the geosynthetic reinforced soil-integrated bridge system under static loading. *Journal of Geotechnical and Geoenvironmental Engineering*, **143**, No. 6, 04017008.
- Zornberg, J. G. (2017). Geosynthetics in roadway infrastructure. *Procedia Engineering*, **189**, 298–306.
- Zornberg, J. G., Roodi, G. H. & Gupta, R. (2017). Stiffness of soil-geosynthetic composite under small displacements: I. Model development. *Journal of Geotechnical and Geoenvironmental Engineering*, **143**, No. 10, 04017075.

The Editor welcomes discussion on all papers published in *Geosynthetics International*. Please email your contribution to discussion@geosynthetics-international.com